Crumpled few-layer graphene: connection between morphology and optical properties

Musikhin, Stanislav; Talebi-Moghaddam, Sina; Corbin, Joel C.; Smallwood, Greg J.; Schulz, Christof; Daun, Kyle J.

Publisher's version / Version de l'éditeur:
https://doi.org/10.1016/j.carbon.2021.06.052
Carbon, 182, pp. 677-690, 2021-06-18

Crumpled few-layer graphene: correlation between morphology and optical properties

Stanislav Musikhin[a,b], Sina Talebi-Moghaddam[a], Joel C. Corbin[c], Greg J. Smallwood[c], Christof Schulz[b], Kyle J. Daun[a]

[a]Department of Mechanical and Mechatronics Engineering, University of Waterloo, Waterloo, ON, Canada
[b]IVG, Institute for Combustion and Gas Dynamics – Reactive Fluids, and CENIDE, Center for Nanointegration Duisburg Essen, University of Duisburg-Essen, 47048 Duisburg, Germany
[c]Metrology Research Centre, National Research Council Canada, Ottawa, ON, Canada

CONTACT: Stanislav Musikhin stanislav.musikhin@uwaterloo.ca Department of Mechanical and Mechatronics Engineering, University of Waterloo, 200 University Avenue West, Waterloo, Ontario N2L 3G1, Canada

ABSTRACT

This study correlates the morphology of gas-phase synthesized crumpled few-layer graphene (cFLG) particles with the optical properties of cFLG aerosols and colloidal suspensions. cFLG morphology was characterized using electron microscopy (TEM, SEM, and tomographic TEM) and aerosol-phase measurements of particle diameter, effective density, and optical properties. The spectral extinction coefficients of FLG were characterized in an ethanol suspension and as an aerosol. The UV-Vis spectra were correlated with the mean particle thickness and the lateral size of the FLG. The cFLG mass absorption cross-section was measured in the aerosol phase and its wavelength dependence was determined. The measured optical properties were simulated using the discrete dipole approximation (DDA) with refractive indices of soot, bulk graphene, and bulk graphite, taken from the literature. In DDA simulations of 3 FLG particles modelled using tomographic TEM data, we found that our nanoparticle FLG measurements were most closely reproduced using the refractive index of bulk graphite. Moreover, a simpler Rayleigh–Debye–Gans model agreed well with the DDA simulations. Further work is needed to understand why the graphite refractive index more closely reproduced the measured properties of nanoparticle FLG.

~~The results are compared to literature data on soot, graphene, and graphite, and reveal that the optical properties of cFLG differ from planar single- or few-layer graphene and more closely resemble graphite, suggesting a substantial influence of the crumpled morphology on the electronic properties. Rayleigh-Debye-Gans theory was shown to agree well with the absorption cross-section trends predicted with DDA, which suggests its applicability for cFLG aerosols.~~

Keywords: crumpled few-layer graphene, gas-phase synthesis, absorption coefficient, mass absorption cross-section, graphene aerosol, graphene suspension, optical properties, discrete dipole approximation.

1. Introduction

Many applications exploit the mechanical, electrical, and optical properties of graphene, which are derived from its highly ordered structure [1,2]. However, recent studies show that the morphology of mass-produced graphene powders and suspensions, and therefore their functionality, often differ considerably from those claimed by the manufacturer [3,4]. The problem of reliable characterization is even more pronounced for crumpled graphene materials, e.g., crumpled few-layer graphene (cFLG) aerosols, one of the most prevalent graphene products [5,6], the properties of which depend strongly on particle morphology [7–9].

Morphologically-dependent properties of crumpled graphene are also needed to understand its potential adverse health effects due to occupational and environmental exposure, and its climatic impact when released into the atmosphere. Currently, there is little consensus on the potential hazards of graphene materials [10–13], in part due to incomplete knowledge about its morphology [11]. Several morphological parameters must be known to predict graphene toxicity and lung deposition efficiency, including the particle lateral dimension, aerodynamic diameter, surface area, and thickness, i.e., number of graphene layers. Also, most previous studies are limited to flat graphene materials, with comparatively little information available on crumpled graphene [11,13]. To understand the role of crumpled graphene aerosol as a climate-forcing agent, climate-relevant spectroscopic properties, such as particle absorption efficiency and the single scattering albedo, should be accurately measured and their dependence on particle morphology investigated.

To date, there is a lack of experimental and theoretical data on the optical properties of crumpled graphene materials. To the best of our knowledge, the only previously reported data is by Zangmeister et al. [14], who measured the mass absorption cross-sections of crumpled few-layer graphene aerosols with a photoacoustic spectrometer and compared their results with other light-absorbing carbon aerosols. They did not model their aerosols in detail.

In this study, we deploy experiments and modeling to characterize the interplay between morphology and optical properties for cFLG suspensions and aerosols. The paper is organized as follows: First, we present a comprehensive morphological analysis of cFLG aerosols: shape, thickness, and distributions of lateral size and aspect ratio, mass, and the mobility and aerodynamic diameters. Next, the optical properties of cFLG suspensions and aerosols are presented: wavelength-resolved extinction and absorption coefficients, mass absorption and extinction cross-sections, and the single scattering albedo. Finally, we model the optical properties of cFLG aerosols and suspensions through Rayleigh–Debye–Gans theory and numeric DDA simulations using geometries derived from tomographic transmission electron microscopy (TEM) on cFLG nanoparticles. The data presented in this work will be useful for the interpretation of optical

measurements on colloids and aerosols of crumpled graphene, and modeling of its climate and health effects.

2. Experimental Procedure

Crumpled few-layer graphene (cFLG) was synthesized from ethanol vapor in a substrate-free gas-phase microwave plasma reactor, as described in detail in Refs. [15,16]. *Ex situ* analysis of the graphene powder revealed high crystallinity and chemical purity. In particular, Raman spectroscopy confirmed that the powder was turbostratic graphene with a low degree of structural disorder, X-ray photoelectron spectroscopy (XPS) showed that the cFLG consists of more than 99 atom% of carbon, over 90 % of which is sp^2-bonded carbon, and transmission electron microscopy (TEM) revealed the crumpled flakes consisting of arbitrarily oriented graphene stacks of less than ten layers [15,16].

The cFLG powder was dispersed in ethanol (≥ 99.5 %) and ultrasonicated for at least 15 minutes. The suspension was then nebulized using a Collison nebulizer (TSI Inc., Model 3076) in recirculation mode, with filtered air at an absolute pressure of 241 kPa as the motive gas. The particle number concentration and the particle size distribution of the suspension were found to remain stable for the several-hours duration of one day's experiments. The nebulized cFLG–ethanol aerosol then passed through a dilution column equipped with a 0.071 cm impactor (TSI Inc., long DMA column). The dilution column serves two purposes: it controls the particle number concentration and evaporates some of the ethanol [17]. The diluted aerosol then flowed through a catalytic stripper (Catalytic Instruments, CS10) operated at 350 °C to evaporate and oxidize semi-volatile impurities including the remaining ethanol. This oxidation produced water vapour, which was removed afterwards by passing the aerosol through a diffusion dryer. The aerosol entering the diffusion dryer remained above the dewpoint even at room temperature. The impact of heating the aerosol inside the catalytic stripper on the particle morphology and the optical properties was negligible; the particle mobility diameter (d_m) distributions and single scattering albedo (SSA) measured with and without the catalytic stripper in the setup were not significantly different (Figure SX).

The aerosol was then directed through one of the three configurations shown in Figure 1. The configuration in Figure 1a was used to measure the particle mobility and aerodynamic (d_{ae}) diameter distributions; the configuration in Figure 1b was used to measure the wavelength-resolved optical extinction coefficient ($b_{ext,\lambda}$) of the dried cFLG aerosol and to collect particles for electron microscopy analysis; and the configuration in Figure 1c was used to measure the cFLG mass absorption cross-section (MAC) at 660 nm and is comparable to the setup used by Corbin et al. (2021).

The devices were connected using electrically conductive carbon-impregnated silicone tubing to minimize size-dependent electrostatic particle losses, which could otherwise bias the measured size distributions. Particle losses were estimated by flowing the aerosol through tubes of different lengths and

then measuring the particle number concentrations and d_m distributions with the scanning mobility particle sizer. We detected negligible particle losses at the experimental conditions, i.e., flowrates and temperatures, for particles larger than 50 nm, which pertain to cFLG particles as described below. All instrument flows were measured using a Gilibrator-2 flow standard (Sensidyne LP) and corrected for the temperature and pressure.

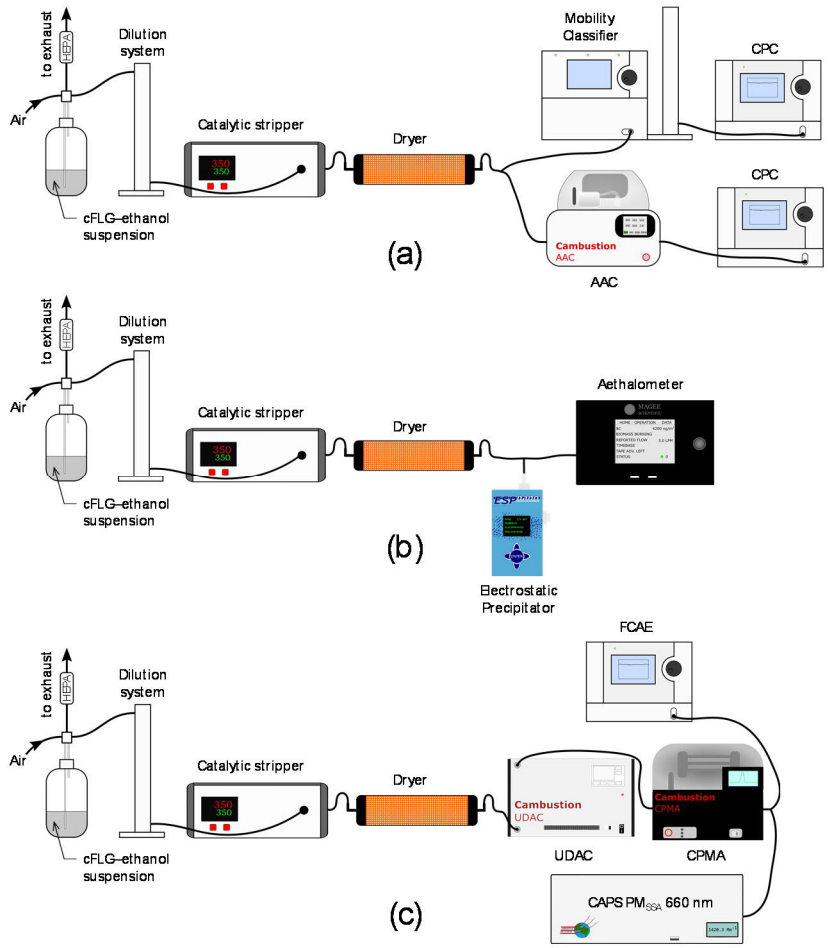

Figure 1. Experimental configurations used for crumpled few-layer graphene (cFLG) aerosol characterization. HEPA: high-efficiency particulate air filter, AAC: aerodynamic aerosol classifier, CPC: condensation particle counter, UDAC: unipolar diffusion aerosol charger, CPMA: centrifugal particle mass analyzer, FCAE: Faraday cup aerosol electrometer, CAPS PM_{SSA}: cavity-attenuated phase-shift monitor.

2.1 Particle morphology measurements

A suite of complementary aerosol instruments and imaging techniques were deployed to characterize the morphology of the gas synthesized cFLG flakes.

Aerosol mobility and aerodynamic diameter distributions were measured using a mobility classifier and an aerodynamic aerosol classifier (AAC), both equipped with a condensation particle counter (CPC), and

arranged in tandem as shown in Figure 1a. The particle mobility diameter is equivalent to the diameter of a sphere having the same electrical mobility and is measured by the balance of electrical and drag forces, while particle aerodynamic diameter is the diameter of a sphere of density 1 g/cm^3 with the same terminal settling velocity. The combination of a mobility classifier/CPC is known as a scanning mobility particle sizer (SMPS). Both the SMPS and AAC were calibrated using spherical polystyrene latex particles of known diameter. In this configuration, the SMPS was equipped with an X-ray bipolar charger and consisted of an electrostatic classifier (TSI Inc., TSI model 3082) with a 0.071 cm impactor (D_{50} cut-point diameter 600 nm), a long differential mobility analyzer column (DMA), and a CPC (TSI Inc., TSI model 3776). The size measurement range was 15 to 700 nm with the sample flow of 0.32 standard liters per minute (slm, defined at 273.15 K and 1 bar) and the sheath-gas flow of 3.2 slm, resulting in a mobility-diameter resolution $R_d = Q_{sheath}/Q_{sample} = 10$. The data were analyzed by the Aerosol Instrument Manager software (TSI Inc., AIM, ver. 10.1), which employs the inversion algorithm by Wiedensohler [18] that accounts for instrument function, diffusion losses, and multiple charging. The uncorrected and corrected mobility diameter distributions are compared in the Supplementary Information (Figure SX). The AAC (Cambustion Ltd.) classifies particles by their aerodynamic diameter based on the balance between centrifugal and drag forces. The AAC aerodynamic size range was set to 23–570 nm with a resolution $R_s = 6.7$. The AAC data were deconvoluted using the algorithm by Johnson et al. [19]. To ensure the cFLG–ethanol suspension stability in terms of particle size distribution, i.e., to exclude the influence of particle precipitation in the nebulizer, the SMPS and AAC scans were performed multiple times before and after the measurements.

The aerosol morphology was additionally analyzed with transmission electron microscopy (TEM, JEOL Ltd., JEM 2200FS, operated at 200 kV), scanning electron microscopy (Hitachi Inc., SEM, S-5200, operated at 30 kV), and tomographic TEM (FEI Titan 80-300 LB). The sampling scheme is shown in Figure 1b. A high-efficiency electrostatic precipitator (Dash Connector Technology Inc., ESPnano model 100) was used to collect the particles onto a 300-mesh copper grid with a carbon support film [20]. For the tomographic imaging, the grid holder was tilted by the step-angle of 2° between the ranges of –60° to +70°. Open source Tomviz software [21] was used for the volume reconstruction using the weighted back-projection algorithm.

2.2 Optical property measurements

The wavelength-resolved aerosol extinction coefficients, $b_{ext,\lambda}$, were measured using an aethalometer (Magee Scientific, model AE33), as shown in Figure 1b, and using a UV-Vis spectrophotometer (Varian Inc., Cary 4000) for the 0.0005 wt.% cFLG–ethanol suspension. The aerosol absorption coefficient, $b_{abs,660}$, was measured at 660 nm using a cavity attenuated phase shift spectrometer (Aerodyne Inc., model CAPS

PM_{SSA} 660 nm), as shown in Figure 1c. The CAPS PM_{SSA} is a well-characterized technique for the measurement of aerosol light absorption [cite], but does not provide spectral information. In contrast, the aethalometer utilizes seven LEDs centered at wavelengths ranging from 370 to 950 nm and can be calibrated in real time using the CAPS PM_{SSA}. The sheath-to-sample flow rates ratio used in the dilution column was adjusted to improve the signal-to-noise ratio for these experiments: a sample flow of 0.8 slm was diluted with 5.46 slm of sheath airflow for the aethalometer, while a sample flow of 1.8 slm was diluted with 2.6 slm of sheath airflow for the CAPS PM_{SSA}.

In the aethalometer, the aerosol sample is deposited upon a filter tape and irradiated. The light transmitted through the particle-loaded filter relative to the unloaded filter is measured and used to calculate the light extinction coefficient of the sample via the Beer–Lambert law. The measured $b_{\mathrm{ext},\lambda}$ can be corrected to the $b_{\mathrm{abs},\lambda}$ using the wavelength-independent scattering correction factor caused by the multiple scattering within the filter fibers. Therefore, $b_{\mathrm{ext},\lambda}$ should have the same wavelength dependence as $b_{\mathrm{abs},\lambda}$. Further details on the correction factor are given in the Supplementary Information.

The cFLG aerosol absorption Ångström exponent (AAE_{cFLG}) was calculated from the wavelength-resolved $b_{\mathrm{abs},\lambda}$ data. The AAE defines the wavelength power-law dependence of the $b_{\mathrm{abs},\lambda}$:

$$b_{\mathrm{abs},\lambda} \propto \lambda^{-\mathrm{AAE}}, \tag{1}$$

and has been shown to be sensitive to particle morphology and chemical composition, i.e., molecular structure [22–24]. Thus, it is commonly used to characterize an aerosol type. For example, the AAE of small black carbon particles is usually close to unity, while the AAE of light-absorbing organic usually exceeds unity [25]. In the case of particles that absorb and emit in the Rayleigh regime, the spectral dependence of the aerosol absorption is usually expressed as

$$b_{\mathrm{abs},\lambda} \propto E\left(\mathbf{m}_\lambda\right) / \lambda, \tag{2}$$

where

$$E\left(\mathbf{m}_\lambda\right) = \mathrm{Im}\left[\frac{\mathbf{m}_\lambda - 1}{\mathbf{m}_\lambda + 2}\right] \tag{3}$$

is the absorption function and $\mathbf{m}_\lambda$ is the complex refractive index of the material normalized by the refractive index of the embedding material.

The MAC measurements were conducted using a CAPS PM_{SSA} monitor on cFLG aerosols of known mass concentration generated using a CPMA-Electrometer Reference Mass System (CERMS), comprised of a unipolar diffusion charger (UDAC, Cambustion Ltd.) [26], centrifugal particle mass analyzer (CPMA,

Cambustion Ltd.), and Faraday cup aerosol electrometer (FCAE, TSI Inc., model 3068B). This CERMS configuration and its principle of operation have been described elsewhere [27]. The UDAC was operated at the ion concentration–time product of 4×10^{13} ions s/m^3 and a sample flow of 2.14 slm. The charged particles were measured with a CPMA, which classifies particles based on the balance between centrifugal and electrostatic forces [28]. The CPMA was operated at a mass flow rate of 2.14 slm and a resolution $R_m = 10$. Measurements were carried out at CPMA setpoints (M) in the range of 0.1–0.5 fg per elementary charge. The CPMA setpoint is directly proportional to the average mass of the transmitted graphene particles in our experiments [Corbin2021] and provides insight into the possible mass-dependent properties of graphene. For a certain CPMA setpoint, particles of different mass-to-charge ratios are able to pass through the instrument, as defined by the instrument transfer function. The FWHM of the CPMA transfer function was calculated as $0.4M$ following the finite-difference approach by Sipkens et al. [29] assuming single-charged spherical particles of constant density and a flow with a parabolic velocity profile. After the CPMA, the classified aerosol was split between the CAPS PM_{SSA} monitor and a Faraday cup aerosol electrometer (FCAE, TSI Inc., model 3068B). Both instruments were operated with an aerosol flow rate of 1.07 slm. The FCAE measures the aerosol charge concentration, which enables absolute mass concentration measurements according to [28]

$$m_{\text{total}} = m_0 + \frac{M \cdot I}{Q \cdot e}, \tag{4}$$

where m_0 is the mass concentration of the uncharged particles, M is the mass setpoint of the CPMA, I is the detected aerosol current, Q is the sample flow, and e is the elementary charge. The FCAE only detects charged particles, so the presence of uncharged particles will bias the mass concentration measurements and consequently the calculated MAC values [30]. Therefore, the concentration of uncharged particles was probed downstream of the UDAC using an electric precipitator (ESP, Cambustion Inc.) combined with a CPC prior to the experiments and was found to be <100 particles/cm^3, which is <1 % of the total particle concentration, and thus considered as negligible.

The CAPS PM_{SSA} monitor is an optical extinction spectrometer, which measures the phase shift in a modulated beam of light due to scattering and extinction. The CAPS PM_{SSA} monitor utilizes a light-emitting diode centered at 660 nm, a sample cell with an integrating-sphere nephelometer, and a vacuum photodiode detector. The particulate extinction coefficient is determined by subtracting the aerosol signal from a filtered (gas-only) signal. The extinction measurement is calibration-free, with a manufacturer-estimated accuracy of 5 % [31]. Aerosol light scattering is measured simultaneously in the integrating sphere and was calibrated before and after the experiments using an aerosol of 200 nm diameter ammonium sulfate particles. The absorption coefficient is found from the difference between extinction and scattering coefficients.

3. Experimental Results

3.1 Particle morphology

Figure 2 shows typical TEM micrographs of aerosolized cFLG nanoparticles that were sampled from the aerosol with the ESPnano, with the TEM stage at angles of −60°, 0°, and 70° relative to incidence. The right side of the graph shows volume-reconstructed particles that will be used in the DDA simulations. Additional electron microscopy images, tomographic videos, and volume reconstructions are given in the Supplementary Information. High-magnification micrographs of the flake edges revealed that the graphene stacks contained fewer than ten layers, which is the definition of few-layer graphene according to the International Standards Organization [32].

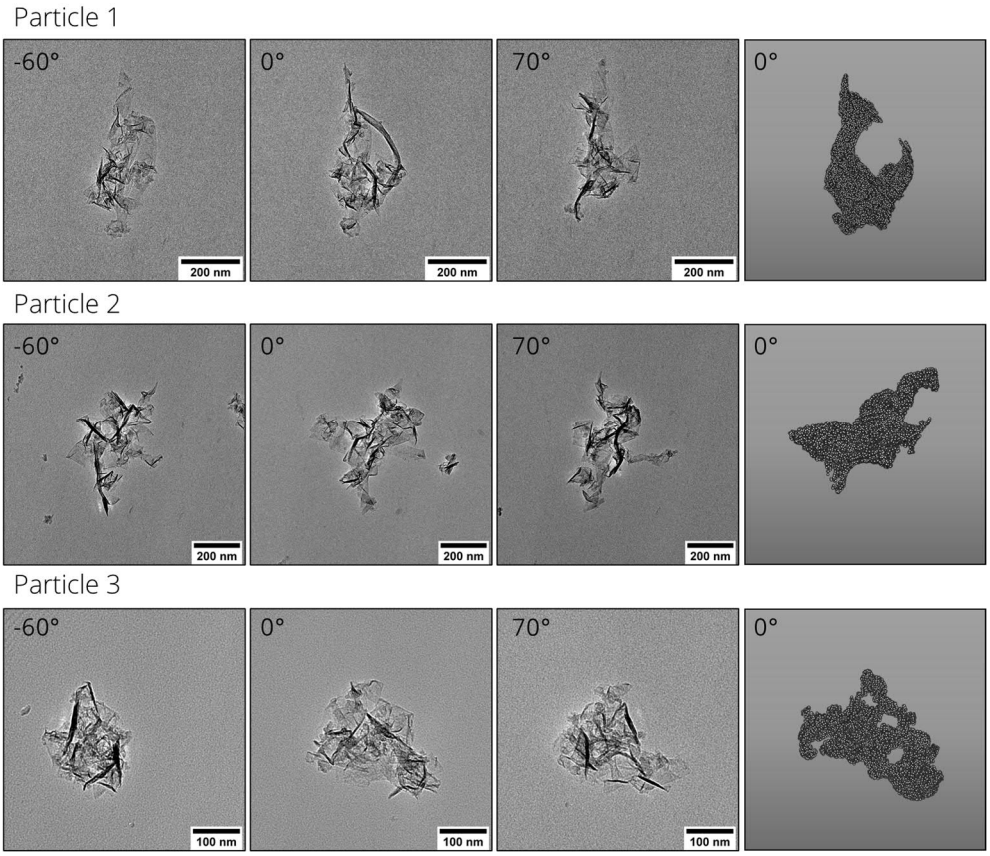

Figure 2. TEM micrographs of the aerosolized cFLG particles at three viewing angles and the volume-reconstructed particles at 0°. Particles are crumpled and thus have a 3D structure. A negligibly small fraction of particles is flat (see Supplementary Information). High-resolution TEM showed that cFLG sheets consist of less than ten layers. Volume-reconstructed particles were meshed and used in the DDA analysis.

Figure 3 shows examples of low- and high-resolution scanning electron microscope (SEM) images and the cFLG lateral size distribution (maximum Feret diameter) derived from 466 particles measured from these images. The size distributions were fit using log-normal distributions to yield a count median diameter (CMD) of 269 nm and a geometric standard deviation (GSD) of 1.54. We also measured the particle aspect ratio as the ratio of major to minor axes of the ellipse. The geometric mean aspect ratio was found to be 1.63 with a GSD of 1.35 (see details in the Supplementary Information). We note that these aspect ratios are not high enough to result in a preferential orientation of the cFLG particles inside the electrostatic classifier [33,34], which would influence their mobility diameter measurements.

To investigate the possible changes in particle size and morphology caused by sample manipulations used in this study, we additionally collected cFLG aerosols *in situ* from the reactor using the ESPnano. Their size and aspect ratio distributions resembled the one in Figure 3 (see Supplementary Information). Thus, we expect no significant change in particle size and crumpledness due to nebulization and consequent aerosol drying. However, to further justify that assumption, additional *in situ* optical measurements are needed, e.g., light scattering [35].

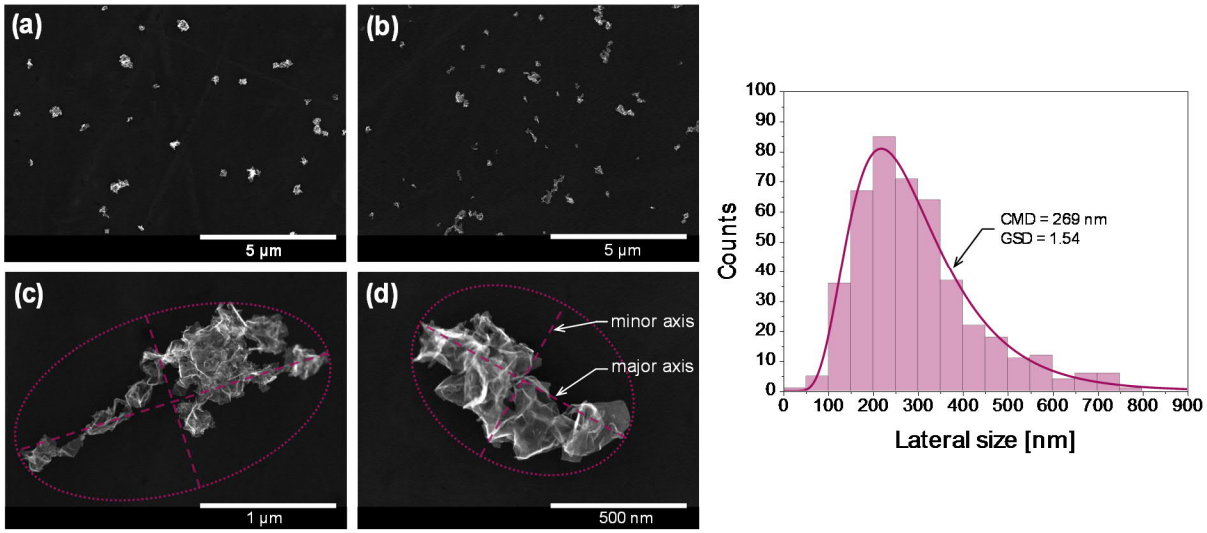

Figure 3. SEM micrographs of aerosolized cFLG particles and the lateral size histogram. The particle lateral size was measured as the major axis of an ellipse inscribing the particle (maximum Feret diameter). The solid line denotes the log-normal fit to the histogram. CMD: count median diameter, GSD: geometric standard deviation.

The cFLG particle-size distributions measured with SEM, SMPS, and AAC are plotted in Figure 4 as probability density functions along with lognormal fits to the data. A bimodal fit was used for the mobility diameter distribution (orange crosses) revealed two separate modes and was split into two log-normal distributions. It is important to keep in mind that these “diameters” incorporate information about distinct physical characteristics of a particle, according to the corresponding measurement principle. Furthermore,

it is necessary to account for the size-dependent efficiencies of the instruments. The corrections to the data are described in the Supplementary Information.

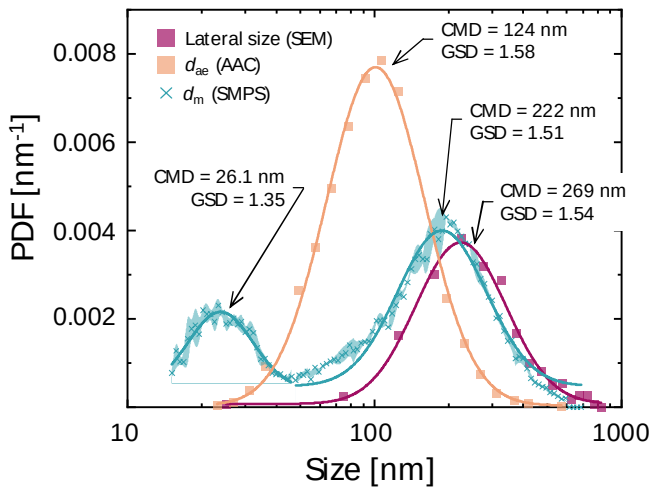

Figure 4. Probability density functions of the aerosolized cFLG particle-size distributions: turquoise crosses – mobility diameter measured with SMPS (filled area corresponds to one standard deviation), orange squares – aerodynamic diameter measured with AAC, plum squares – lateral size measured with SEM. Solid lines show the corresponding log-normal fits to the data. The mobility diameter data (SMPS) were split into two log-normal distributions. CMD: count median diameter, GSD: geometric standard deviation.

Figure 4 shows that the d_m distribution is bimodal with the smaller particles of CMD = 26.1 nm, and the larger particles of CMD = 222 nm. The small particles are likely residues from organic impurities in the ethanol, which may have penetrated through the catalytic stripper due to the very high concentration of ethanol at its inlet. Such impurities are universally observed when nebulizing solid particles and correspond to a very small mass fraction in the original solution [36]. For example, assuming spherical particles of equal density and a nebulizer droplet size of XXXXX, the observed 26.1 nm particles mode would represent a solution impurity of only 1.5 wt%. This hypothesis is also supported by the fact that the SEM analysis did not reveal any particles smaller than 50 nm, suggesting that they were, in fact, volatile, and hence evaporated from the grid surface under a high vacuum. The d_{ae} distribution is unimodal and does not show the volatile particles mode. That is because the AAC detection range was set to 23–570 nm, which corresponds to the d_m range of 40–1040 nm, hence, only the larger mode of particles was observable when using the AAC.

The second mode of the d_m distribution, which corresponds to solid particles, resembles the lateral size distribution. The close similarity between the d_m and the lateral size (maximum Feret diameter) is expected in the free molecular and transition regimes for particles with a "scaling" nature, such as fractal aggregates [37]. The flow regime is defined by the Knudsen number, $Kn = 2\lambda/d_p$, where λ is the gas mean free path, and d_p is the particle physical diameter. The mean free path for air at room temperature and atmospheric

pressure is taken as 67.3 nm [38], and the range of d_p is taken as FWHM of the lateral size distribution, 125–400 nm (Figure 3). Therefore, the measurements occur in the transition regime with $0.3 < Kn < 1.1$. Hence, we suggest, that the standard SMPS system applied on the cFLG aerosols in the free-molecular and transition regimes should give a reasonable lateral size estimate. That result also indicates the "scaling" nature of the gas-phase grown cFLG particles, which is analogous to the fractal dimension of fractal-like aggregates [33]. This is supported by the SEM analysis we performed using the box counting method in ImageJ, FracLac [39], which yielded the scaling exponent between 1.7–1.9 (details available in the Supplementary Information). This result is in good agreement with Ku and Kulkarni [33], who measured the scaling exponent of graphene using TEM to be between 1.85–1.95.

3.2 Optical properties

Figure 5 shows measurements of the extinction coefficients ($b_{ext,\lambda}$) of the cFLG–ethanol suspension and filter-deposited cFLG aerosols as a function of wavelength, as measured by UV-Vis spectroscopy and with the aethalometer, respectively. The data are normalized to 660 nm to enable the comparison.

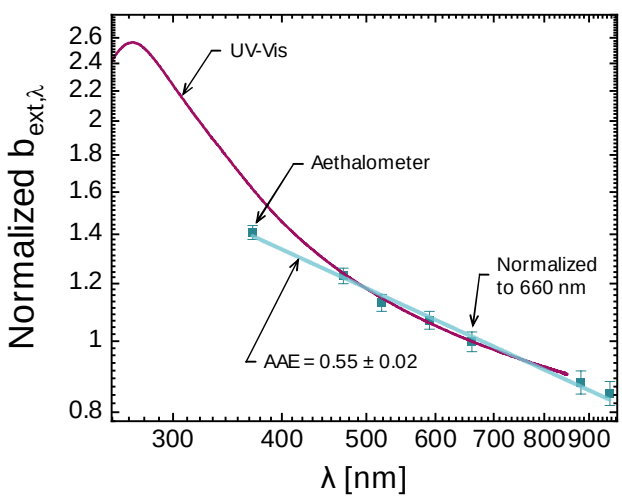

Figure 5. Wavelength-dependent extinction coefficient ($b_{ext,\lambda}$) of an cFLG–ethanol suspension measured by UV-Vis spectroscopy, and of filter-deposited cFLG aerosol measured with an aethalometer. The error bars denote one standard deviation of the mean. The blue straight line denoted as AAE is the linear fit to the aethalometer data. Both datasets are normalized to 660 nm.

The UV-Vis extinction spectrum peaks at 269 nm, which corresponds to π–π^* electronic transitions of C=C bonds and is commonly observed for pure graphene [40,41]. In the case of graphene oxide, the extinction peak blue-shifts towards ~230 nm [41]. The wavelength-independent AAE value of 0.55 ± 0.02 was calculated via a linear fit to the logarithmic aethalometer data shown in Figure 5. The constant AAE value allows us to make an assumption on the wavelength dependence of the absorption function $E(\mathbf{m}_\lambda)$.

For example, the typical AAE for soot and black carbon aerosols equals to one [42], which, according to Eqs. (1) and (2), leads to the constant absorption function over the measurements range. Hence, $AAE_{cFLG} \neq 1$ suggests that $E(\mathbf{m}_\lambda)$ for cFLG aerosols is wavelength-dependent between 370–950 nm.

We extract the mean particle thickness and lateral size from the UV-Vis extinction spectrum of the cFLG–ethanol colloid, using metrics from Backes et al [43]. These authors used a UV-Vis spectrometer equipped with an integrating sphere to measure wavelength-resolved extinction and scattering coefficients of size- and thickness-selected graphene suspensions. They found that the extinction peak position and curvature of the spectrum depend on the lateral size and thickness of the graphene sheets. The correlations were found to be robust when tested against lab and commercial suspensions, different solvents and stabilizers, and particles with different stacking orders. We note that Backes et al. [43] worked with relatively flat graphene nanosheets produced from graphite exfoliation, while in our study, we analyze crumpled 3D-like cFLG particles.

The metrics of particle thickness, i.e., the mean layer number, was established by Backes et al. [43] using the ratio of b_{ext} at the peak to b_{ext} at the long-wavelength region: $\langle N \rangle \pm 15\ \% = 25 \times b_{ext,550}/b_{ext,peak} - 4.2$, which yields $\langle N \rangle = 6.55 \pm 0.98$. The particle thickness can also be estimated using the extinction peak position: $\langle N \rangle = 0.81 \times \lambda_{ext,peak} - 213$, which results in $\langle N \rangle = 4.89$. The UV-Vis inferred mean particle thickness of 5–8 layers is in good agreement with other analyses we performed. In particular, HR-TEM showed that most of the particles are thinner than ten graphene layers, and Brunauer–Emmett–Teller analysis yielded the specific surface area of 300–400 m^2/g [15], which corresponds to 7–9-layer flat graphene nanosheets calculated as $N = 2/(\rho d S)$, where ρ is the graphite density (2.267×10^6 g/m^3), d is the interlayer spacing (0.34×10^{-9} m), and S is the specific surface area.

We also use the UV-Vis extinction curve to estimate the mean lateral size of the particles exploiting the size dependence of the scattering coefficients. While the UV-Vis curve corresponds to the extinction (absorption + scattering), Backes et al. [43] showed that the scattering decay exponent can be inferred from the extinction spectrum in the long-wavelength region (650–800 nm), since absorbance in that region is largely flat, i.e., wavelength-independent. Hence, any wavelength dependence of the extinction curve at wavelengths longer than 650 nm is mainly due to the scattering, and the scattering exponent can be approximated as the extinction exponent, i.e., $b_{ext,\lambda} \propto \lambda^{-n}$. We fit the extinction curve with a power law in the long-wavelength region, $\lambda^{-0.434}$, and calculate the lateral size as $\langle L \rangle = (0.434/2.466)^{-3.05} \approx 200$ nm. This is within the lateral size distribution measured by SEM, as shown in Figure 4. Overall, these results show that UV-Vis spectroscopy on cFLG suspensions can give reasonable estimates of the particle mean thickness and lateral size.

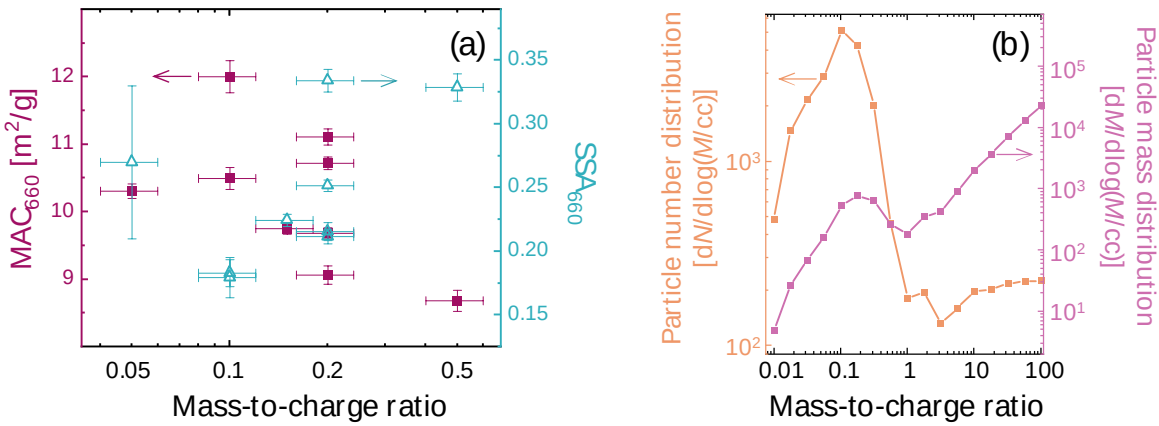

Figure 6. a) MAC and SSA of an cFLG aerosol measured with the CAPS PM_{SSA} at 660 nm versus mass-to-charge ratio (CPMA setpoint). Vertical error bars denote one standard deviation of the mean, horizontal error bars denote FWHM of the CPMA transfer function; b) cFLG aerosol particle number and mass distributions versus mass-to-charge ratio. The arithmetic mean $MAC_{cFLG,\,660}$ is 10.19 ± 1.10 m^2/g.

Figure 6a shows mass absorption cross-section (MAC) and single scattering albedo (SSA) for the cFLG aerosol versus mass-to-charge ratio (CPMA setpoint). The MAC was calculated at 660 nm as $MAC_{660} = b_{abs,660} / m^*$, where m^* is the particle mass concentration measured with CPMA, and $b_{abs,660}$ is the aerosol absorption coefficient measured with CAPS PM_{SSA} at 660 nm. The SSA was calculated as $SSA_{660} = b_{sca,660}/b_{ext,660}$. The calculated MAC arithmetic mean is $MAC_{cFLG,\,660}$ = 10.19 ± 1.10 m^2/g (± 11 %). The $SSA_{cFLG,\,660}$ values are scattered between 0.17–0.33. Figure 6b shows the cFLG aerosol mass distributions in terms of particle number and mass densities, as measured with CPMA in scanning mode. Even though there are some massive particles in the aerosol, most of the particles have a mass-to-charge ratio less than 1, which makes CAPS PM_{SSA} measurements at higher values difficult. Both $MAC_{cFLG,\,660}$ and $SSA_{cFLG,\,660}$ demonstrate no apparent dependence on the mass-to-charge ratio, thus, no mass dependence is expected. Backes et al. [43] came to the same conclusion when measuring the extinction and scattering coefficients of graphene–water suspensions at 660 nm. They calculated SSA_{660} between 0.07–0.18 with no dependence on particle size and thickness, and hence no dependence on mass. The study by Dastanpour et al. [44] on soot particles from an inverted methane/air diffusion flame, on the other hand, reported that MAC_{660} and SSA_{660} values were mass-dependent.

The wavelength dependence of MAC_{cFLG} values can therefore be described using the measured mean $MAC_{cFLG,\,660}$ = 10.19 ± 1.10 m^2/g (Figure 6a) and the AAE_{cFLG} = 0.55 ± 0.02 (cf. Figure 5), resulting in (Figure 7):

$$MAC_{cFLG,\,\lambda} = MAC_{cFLG,\,660}\left(\frac{660}{\lambda}\right)^{AAE_{cFLG}} . \tag{5}$$

~~The resulting $MAC_{cFLG,\lambda}$ calculated for the aethalometer spectral range of 370–950 nm is shown in Figure 7.~~

We also calculated the wavelength-resolved mass *extinction* coefficient of the cFLG–ethanol suspension ($MEC_{cFLG\text{-}ethanol,\ \lambda}$) using the Beer-Lambert law (see Figure 7). At 660 nm $MEC_{cFLG\text{-}ethanol,\ 660} = 5.75 \pm ???$ m^2/g. This value is not significantly different from the $MEC_{660} \approx 5.8\ m^2/g$ previously reported by Backes et al. [43] for a cFLG–water suspension, and is within one standard deviation of literature measurements on light-absorbing carbon aerosols (see inset in Figure 7) [14,42,45], even when MAC recalculated to MEC. However, this is almost half the aerosol $MAC_{cFLG,\ 660} = 10.19 \pm 1.10\ m^2/g$ measured in this study. We see two possible explanations on why MEC could differ when measured in solvent rather than in air. First, this could indicate that the particle morphologies are different between the colloid and aerosol. However, a comparison of TEM micrographs of particles sampled from the cFLG reactor aerosol with the ESPnano with those sampled by drop-casting a droplet of the colloid on the TEM grid reveal no significant differences in particle shape, thickness, and size [15]. Another reason could be the different chemical compositions of the particles. In this study, we used X-ray photoelectron spectroscopy to confirm the chemical purity of the cFLG powder before dispersing it in absolute ethanol (≥ 99.5 %). When nebulized, the aerosol was diluted, thermally oxidized, and dried to remove semi-volatile components. We note that a portion of volatile components persevered in the aerosol in the form of droplets (cf. Figure 4). That indicates a possible coating of cFLG particles in the aerosol, which could lead to the enhanced MAC [46]. To exclude that possibility, additional optical *in situ* measurements on as-synthesized cFLG aerosols are required.

We compare the $MAC_{cFLG,\lambda}$ values reported here with available in the literature data on light-absorbing carbon aerosols [14,42,45,47]. In terms of cFLG, the most relevant work is by Zangmeister et al. [14], who measured the MAC_λ and AAE of crumpled graphene nanoplatelets and thermally reduced graphene oxide (rGO) aerosols with a broadband photoacoustic spectrometer (see Figure 7). They generated the aerosols by nebulizing graphene–water suspensions. At 660 nm, they found the MAC of graphene and rGO to be 6.44 ± 0.09 and $6.85 \pm 0.13\ m^2/g$, respectively, while the corresponding AAEs were 0.74 ± 0.05 and 0.83 ± 0.07 [14]. The discrepancy between the MAC_λ and AAE reported by Zangmeister et al. and the results of the present study could be attributed to different measurement methods that deploy different physical principles and different chemical compositions of graphene samples. The samples in the Zangmeister et al. study were dispersible in water, while chemically pure graphene is hydrophobic. It was not possible to disperse the graphene sample of this study in pure water, which is why ethanol was used instead. Therefore, the data of Zangmeister et al. likely represent two types of graphene oxide. To the best of our knowledge, no other optical properties data are available on graphene or graphite aerosols.

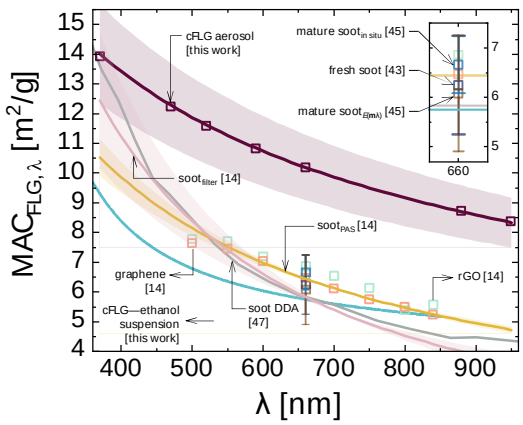

Figure 7. Wavelength-resolved MAC of an cFLG aerosol (plum squares) calculated from the $MAC_{cFLG,\,660} = 10.19 \pm 1.10$ m^2/g and the $AAE_{cFLG} = 0.55 \pm 0.02$ (solid plum line). Shaded areas denote one standard deviation propagated from the MAC_λ and AAE uncertainties. Wavelength-resolved MEC of an cFLG–ethanol suspension is shown as a solid aqua line. Other symbols and lines are the literature MAC data for carbonaceous aerosols. The inset shows the zoomed-in 660 nm part of the graph.

We then compared the optical properties of cFLG with those of soot and black carbon aerosols reported in the literature. Since most literature studies report MAC_λ at a single wavelength, we extrapolated such measurements across the visible spectrum using Eq. (5) and either the reported AAE or an assumed AAE = 1 when no wavelength-resolved data were reported.

We place $MAC_{cFLG,\lambda}$ in the context of three previous reviews of the MAC of soot. Bond and Bergstrom [42] recommended $MAC_{660} = 6.25 \pm 1$ m^2/g for freshly-emitted soot based on 17 historical measurements. Another review by Zangmeister et al. assessed 199 MAC measurements for carbonaceous aerosols [14]. An average of all measurements, removing the outliers with deviation from the mean > 5σ, yielded $MAC_{660} = 6.98 \pm 0.15$ m^2/g and AAE = 0.85 ± 0.09, while an average of only filter-based methods (such as the one used here), again with outliers removed, gives the $MAC_{660} = 5.83 \pm 0.44$ m^2/g and AAE = 1.31 ± 0.28 [14]. A more recent review by Liu et al. [45] reported the $MAC_{660} = 6.66 \pm 0.58$ m^2/g based on ten studies that measured both absorption and mass using *in situ* techniques. Liu et al. [45] also reviewed studies on mature soot $E(\mathbf{m}_\lambda)$ measurements and reported the inferred from that the average $MAC_{660} = 6.08 \pm 1.17$ m^2/g. Kelesidis et al. [47] reported the $MAC_{660} = 5.84$ m^2/g based on soot DDA simulations. As one can see in Figure 7, the large body of literature on carbonaceous aerosols shows MAC_{660} values between 5–7 m^2/g.

Overall, we consider $MAC_{cFLG,\lambda}$ to be larger than MAC_λ of soot and black carbon, i.e., cFLG aerosols absorb light in the 370–950 nm range more efficiently than soot. That observation is also supported by a recent laser-induced incandescence (LII) study [15], which suggested that cFLG particles have a larger

absorption cross-section at the laser excitation wavelength of 1064 nm compared to soot, based on the observed peak pyrometric temperatures of the two nanoparticle types reached after illumination with the dame laser fluence. We should also note that in the present study the nanoparticles were dispersed in ethanol, nebulized, dried, and then sampled on a filter tape; any of these steps could potentially influence the cFLG morphology and thus the optical properties. Although the TEM results indicate that such changes were minimal, future work will focus on *in situ* measurements to avoid possible biases due to the aerosol manipulations.

4.0 Discrete Dipole Approximation and Rayleigh Debye Gans theory

Further insight into the connection between cFLG morphology and the optical properties can be obtained through Rayleigh–Debye–Gans (RDG) theory and the discrete dipole approximation (DDA) [48,49]. In DDA, matter is approximated as an ensemble of coupled "numerical" dipoles (each of which represent thousands of physical dipoles) that interact with each other in the presence of an oscillating electromagnetic field. The spectral cross-sections and the scattering phase function are then calculated by combining dipole fields and the field of the irradiation far away from the object. The result is a rigorous, albeit computationally-intensive, simulation of how an incident electromagnetic (EM) wave interacts with matter.

RDG theory, in contrast, provides a more straightforward, analytically closed-form expression for the absorption and scattering cross-sections. The foundation of this approach is the electrostatic approximation, in which the phase variation of the electromagnetic field inside the particle is assumed to be negligible. Accordingly, each dipole interacts "in phase" with the EM wave, and thus their contribution to the overall absorption and scattering cross-sections can simply be superimposed. In particular, the spectral cross-sections approximated in RDG theory are [50]:

$$C_{\mathrm{abs},\lambda} = \frac{\pi^2 d_{\mathrm{V}}^3 n_{\mathrm{med}}}{\lambda} E\left(\mathbf{m}_\lambda\right), \tag{6}$$

and

$$C_{\mathrm{sca},\lambda} = \frac{2\pi^5 d_{\mathrm{V}}^6 n_{\mathrm{med}}^4}{3\lambda^4} F\left(\mathbf{m}_\lambda\right), \tag{7}$$

where d_{V} is the volume equivalent diameter of an cFLG particle, n_{med} is the index of refraction of a dielectric medium, $E(\mathbf{m}_\lambda)$ is given by Eq. (3), and

$$F\left(\mathbf{m}_\lambda\right) = \left|\frac{\mathbf{m}_\lambda - 1}{\mathbf{m}_\lambda + 2}\right|^2 . \tag{8}$$

The spectral extinction efficiency is then

$$Q_{\mathrm{ext},\lambda} = Q_{\mathrm{sca},\lambda} + Q_{\mathrm{abs},\lambda} = \frac{4\left(C_{\mathrm{sca},\lambda} + C_{\mathrm{abs},\lambda}\right)}{\pi d_{\mathrm{V}}^{2}}. \tag{9}$$

The optoelectronic properties of graphene are highly anisotropic due to the two-dimensional confinement of electrons through π-bonds and the specific band structure of graphene [51]. This is reflected by distinct in-plane and off-plane refractive indices of graphene [52–56]. It is also possible that the optical properties of cFLG particles differ from a single- or few-layer plane graphene on a substrate due to their complex "non-flat" morphology. In the absence of data on crumpled graphene materials, we extended the analysis towards graphite refractive indices. The refractive indices of graphene and graphite used in this study are shown in Figure SX in the Supplemental Material, and the corresponding $E(\mathbf{m}_\lambda)$ values are shown in Figure 8. The datasets summaries are given in Table 1.

We applied DDA to three cFLG particles obtained from tomographic TEM reconstructions, as shown in Figure 2. The TEM-inferred 3D shapes contained artifacts caused by the tomographic reconstruction algorithm. Therefore, the 3D objects were initially meshed with a uniform DDA mesh with a lattice size parameter of 0.35 nm, which is the approximate thickness of monolayer graphene. A cut-off radius of 30 nm was then defined for each dipole, and all the dipoles inside this radius were chosen. If the number of dipoles contained within this radius is less than 3200, the dipole is removed. This process is repeated for all the dipoles. The parameters for this algorithm were adjusted to make the final 3D mesh visually similar to the tomographic results and achieve a single dipole thickness where single-layer graphene was detected with tomographic TEM. The 3D shape files and the corresponding final DDA meshes can be found in the Supplementary Information to this article. To account for graphene optical anisotropy, three methods for assigning the polarizability tensor of each dipole were compared: (i) assuming random orientation for each dipole; (ii) assuming fixed orientation for all dipoles; and (iii) the plane fit approach described in the Supplementary Information. As shown in Figure SX in the Supplemental Material, all three approaches produced almost identical normalized $Q_{\mathrm{abs},\lambda}$ spectra, hence, we use the plane-fit approach for all subsequent analyses.

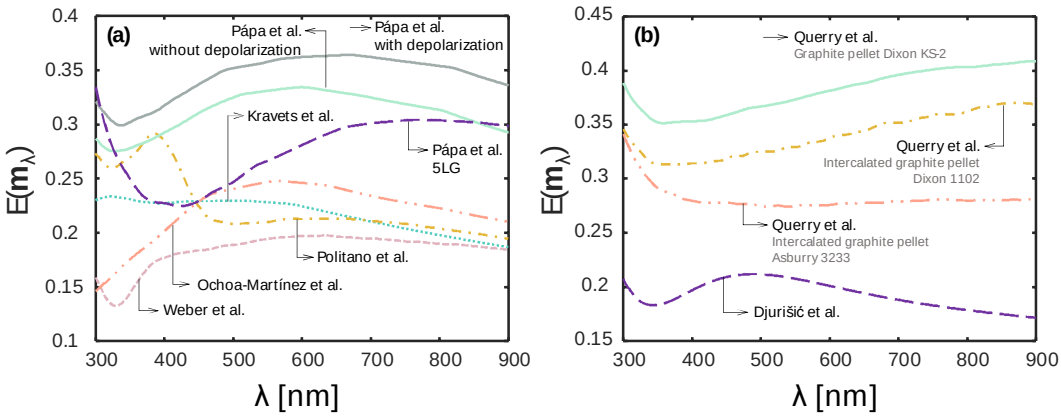

Figure 8. Graphene (a) and graphite (b) absorption functions as calculated from the refractive indices from the literature. The medium in all cases was air (n_{med} = 1). The summary of the studies is given in Table 1.

Table 1. Refractive indices of graphene and graphite used in the DDA calculations.

Author	Material	Methodology
Kravets et al. [52]	Single-layer graphene	Ellipsometry analysis of single-layer graphene placed on an amorphous quartz substrate
Weber et al. [53]	Single-layer graphene	Ellipsometry measurements applied to a mechanically exfoliated graphene flake on a silicon wafer with SiO_2 on top
Politano et al. [54]	Bilayer graphene	Ellipsometry was applied to a CVD-grown bilayer graphene produced by multiple transfers on SiO_2/Si and polyethylene terephthalate substrates
Ochoa-Martínez et al. [55]	Single-layer graphene	Ellipsometry was applied to graphene films grown on copper substrates and transferred onto a SiO_2/Si substrate
Pápa et al. [56]	Single- and five-layer graphene	Ellipsometry applied to single- and five-layer graphene on a SiO_2 substrate. The influence of depolarization was investigated
Djurišić et al. [57]	Highly-oriented pyrolytic graphite	The optical properties of graphite are modeled with a modified Lorentz–Drude model. The model showed good agreement with results found by ellipsometry measurements for highly-oriented pyrolytic graphite
Querry [58]	Various graphite pellets	Reflectance spectra of various 13-mm diameter pressed disk-shaped graphite pellets were acquired. The refractive index was inferred by using the Kramers–Kronig method [59]. Three different refractive indices were used in this study: (1) graphite pellet, Dixon KS-2; (2) intercalated graphite pellet, Dixon 1102; (3) intercalated graphite pellet, Asbury 3222

The light scattering model under the RDG approximation was developed for anisotropic spheres by Pecharroman et al. [60], but it does not strictly apply to the complex morphology of cFLG particles. However, as we expect negligible absorption and scattering contributions from the off-plane refractive index (Figure SXc in the Supplemental Material), normalized cFLG cross-sections could be approximated with RDG using the in-plane refractive index of the scatterer only.

Figure 9 compares the extinction spectra derived using the RDG approximation against DDA simulations for the geometries of three cFLG particles shown in Figure 2. The refractive index data of single-layer graphene from Kravets et al. [52] and the refractive index of air as the surrounding medium (n_{med} = 1) were used. The RDG approximation by its nature is unable to account for the influence of particle

orientation on the optical properties, so RDG predictions are compared with orientation-averaged DDA results. The relative difference between RDG and DDA decreases from 33 % at λ = 300 nm to 9 % at λ = 1100 nm, which is caused by a decrease in the phase shift parameter $\rho = \pi d_V|\mathbf{m}_\lambda|/\lambda$. The normalized plot in Figure 9b also shows that the RDG can predict the spectral cross-section slope of DDA calculations. Therefore, RDG can be used as an approximation to evaluate averaged spectral cross-section of cFLG particles, especially at near-infrared wavelengths, which is often used in laser-induced incandescence [15].

The DDA simulations were repeated for Particle 1 (Figure 2, top row) using a refractive index independent of wavelength to assess whether the cFLG particle absorbs and emits in the Rayleigh regime. Three complex refractive indices were chosen from Kravets et al. [52]: $\mathbf{m}_{300\text{nm}} = 2.656 + 1.879\text{i}$, $\mathbf{m}_{600\text{nm}} = 2.566 + 1.382\text{i}$, and $\mathbf{m}_{900\text{nm}} = 2.912 + 1.596\text{i}$. If the RDG model is valid, it is expected from Eq. (6) and Eq. (9) that $\lambda Q_{\text{abs},\lambda}$ be wavelength independent. Figure 10 shows that $\lambda Q_{\text{abs},\lambda}$ drops by only 1.2 % from 300 nm to 1100 nm, indicating that the RDG model is indeed a valid approximation to predict the slope of $Q_{\text{abs},\lambda}$ for graphene in the visible and near-infrared. To minimize the relative error, we proceed with DDA simulations in further analyses.

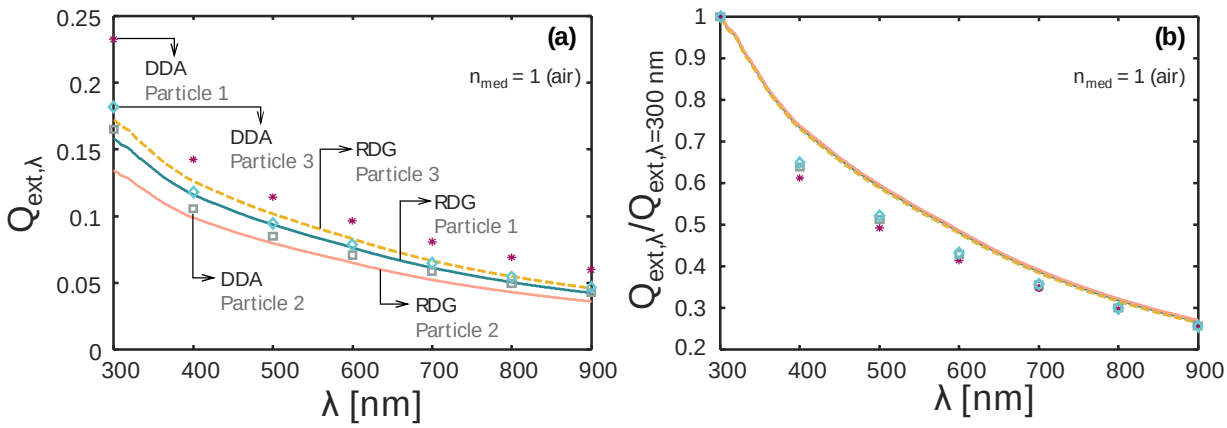

Figure 9. Verifying the RDG predictions of absolute (a) and normalized (b) extinction efficiencies for cFLG Particles 1, 2, and 3 with DDA. The relative difference between RDG and DDA decreases from 33 % at λ = 300 nm to 9 % at λ = 1100 nm. The normalized plot (b) also shows RDG capability to predict the averaged spectral cross-section of cFLG particles, primarily at near-infrared. Calculations were performed for n_{med} = 1.0 (air). The refractive index of graphene from Kravets et al. [52] was used for these calculations.

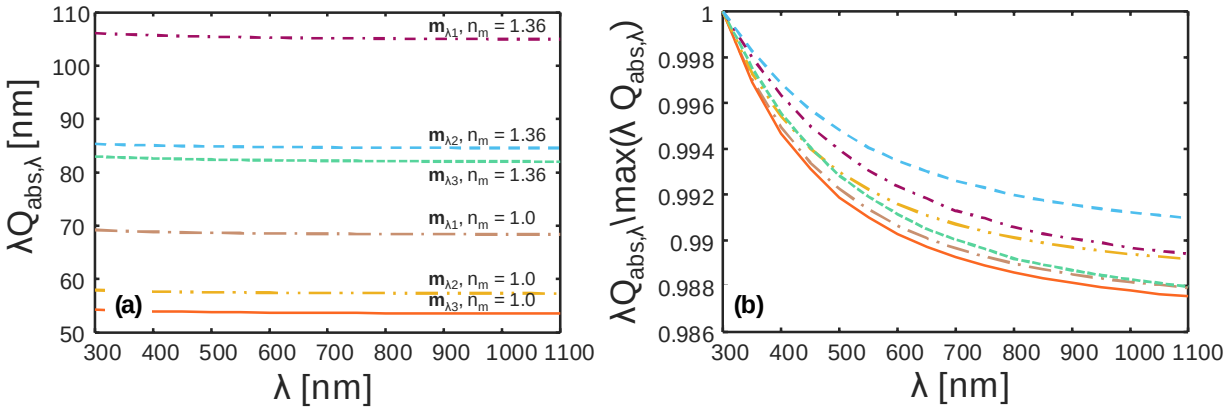

Figure 10. Absolute (a) and normalized (b) $\lambda Q_{abs,\lambda}$ values calculated using DDA with fixed refractive indices at λ_1 = 300 nm, λ_2 = 600 nm, and λ_3 = 900 nm from [52]. Refractive index of a medium: n_{med} = 1.36 (ethanol), n_{med} = 1.0 (air). $\lambda Q_{abs,\lambda}$ drops by only 1.2 % from 300 nm to 1100 nm, indicating that the RDG model could be a valid approximation to predict the slope of $Q_{abs,\lambda}$ for cFLG particles.

Figure 11 compares the normalized values of experimentally measured extinction efficiencies of the cFLG–ethanol suspension (UV-Vis) and the cFLG aerosol (aethalometer) against DDA simulations using different graphene in-plane refractive indices. The off-plane refractive index from Kravets et al. [52] was adopted. There is a considerable variation in the results based on the chosen refractive index. The closest fit to the UV-Vis data was achieved using the single-layer graphene data from Pápa et al. [56] with no influence of depolarization observed. The DDA curve for five-layer graphene [56], though having a similar thickness as the cFLG particles in this study, did not improve the fit to the experimental data. Moreover, none of the DDA simulations resemble the aethalometer measurements carried out on cFLG aerosols. This

could indicate that the morphology of colloidal cFLG particles are closer to that of plane graphene sheets, while aerosolized cFLG particles have complex crumpled nature, which alters the graphene electronic structure [61,62], and thus, the optical properties. To determine the morphology of the particles in suspensions, optical *in situ* measurements are necessary, such as multi-angle elastic light scattering [35,63].

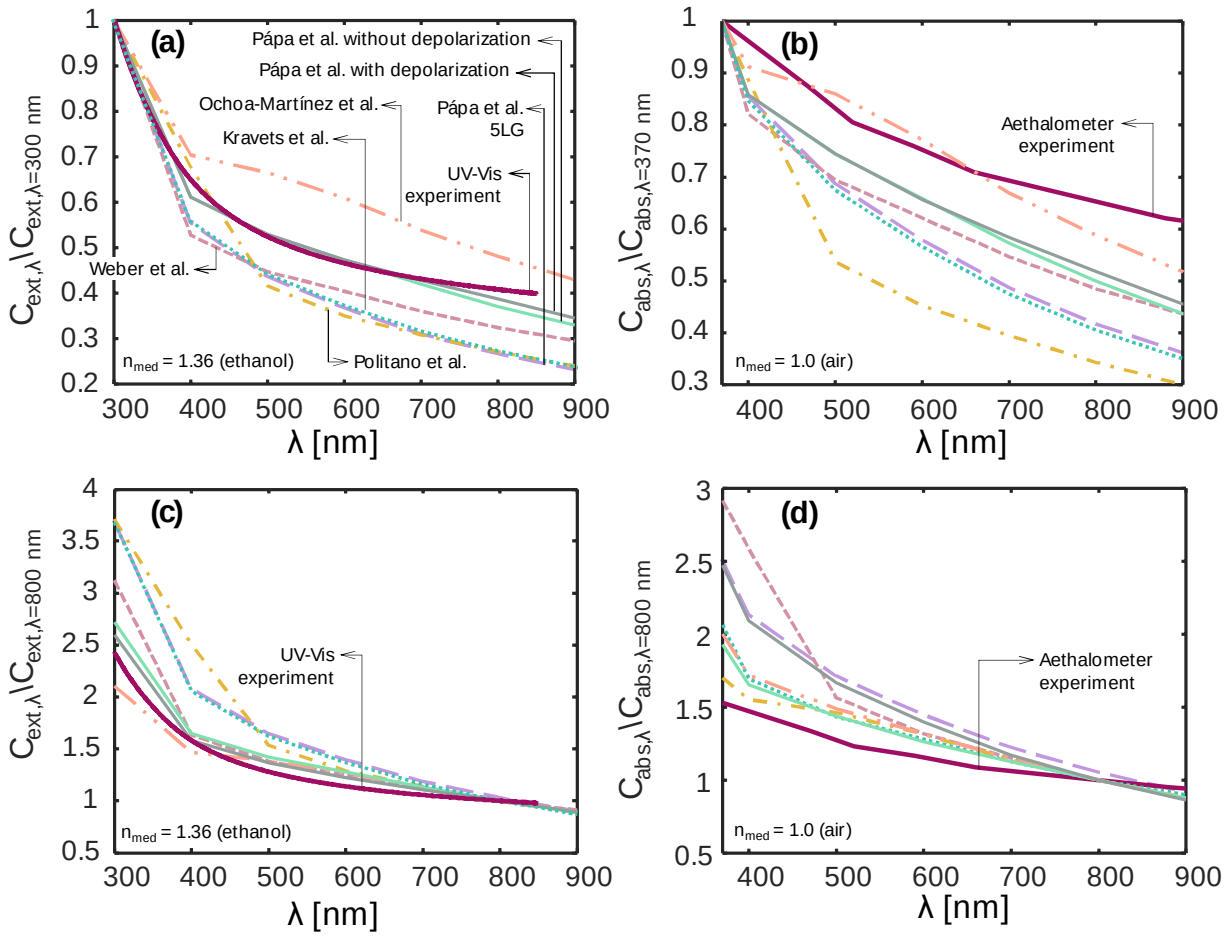

Figure 11. Comparing DDA simulations for different graphene refractive indices with: (a), (c): UV-Vis extinction measurements on the colloid and (b), (d): aethalometer measurements on the aerosol. The curves in (a) and (b) are normalized to 300 nm, in (c) and (d) to 800 nm. The refractive index of the media are taken to be 1.36 (ethanol) and 1.0 (air). The refractive index from Pápa et al. [56] provides the closest fit to the UV-Vis data, while no refractive index results in a reasonable fit to the aethalometer data.

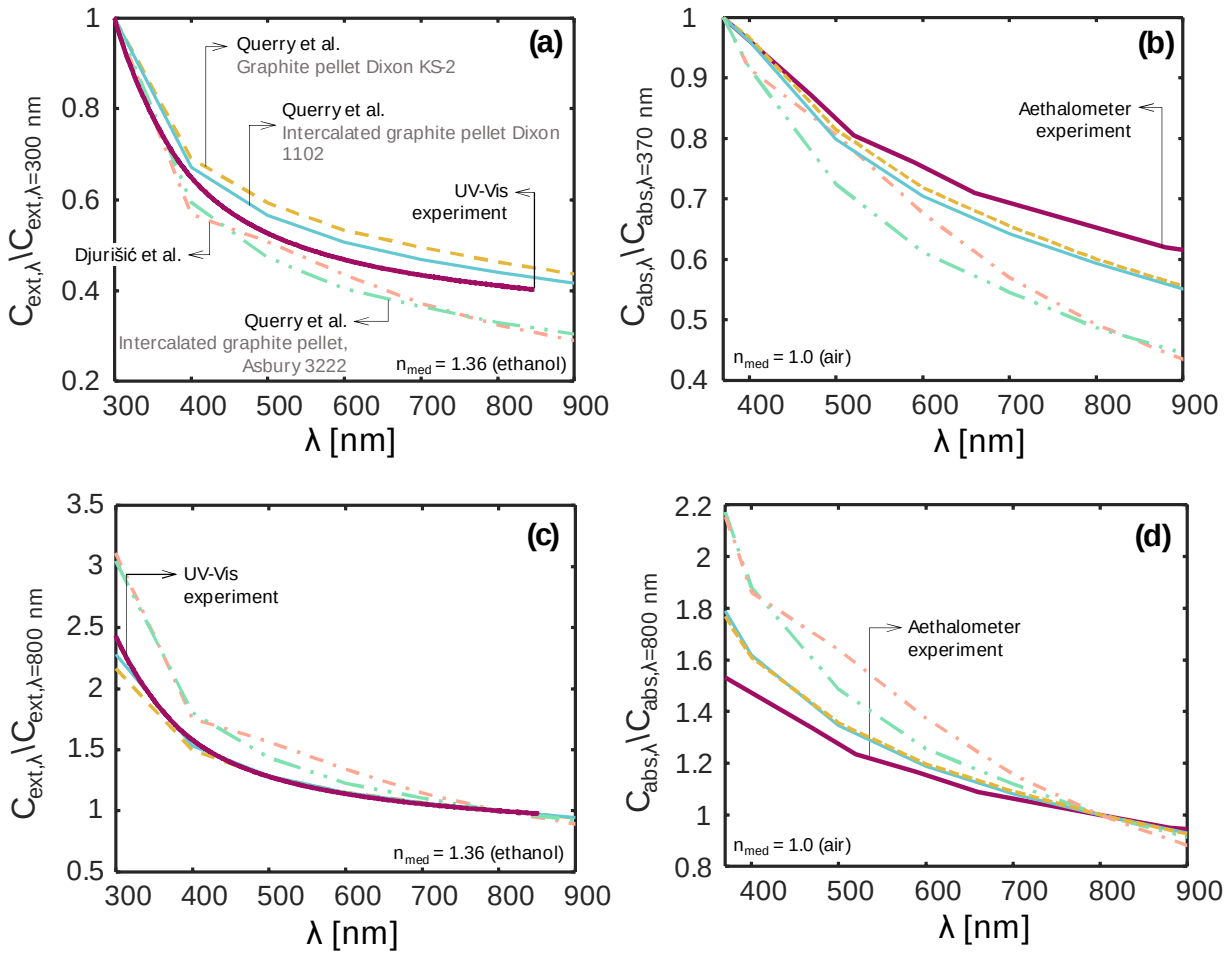

Figure 12. Comparing DDA results for different graphite refractive indices with: (a) and (c): UV-Vis extinction measurements on the colloid and (b) and (d): aethalometer measurements on the aerosol. The curves in (a), (b) are normalized to 300 nm, in (c), (d) to 800 nm. The refractive index of the media are taken to be 1.36 (ethanol) and 1.0 (air). The graphite refractive indices for graphite pellets (Dixon KS-2) and intercalated graphite pellets (Dixon 1102) from Querry [58] provide the closest fit for experiments in both media.

The comparison of UV-Vis and aethalometer measurements with DDA predictions using graphite refractive indices is shown in Figure 12. The DDA simulations predict the experimental UV-Vis curve and reasonably well describe the experimental aethalometer curve. Overall, the difference between the graphite DDA predictions and the measurements is smaller compared to that of graphene DDA (Figure 11). The best-fitting simulations for cFLG in both media provide the graphite refractive indices of Dixon KS-2 pellets and Dixon 1102 intercalated graphite pellets from Querry [58].

Overall, these results suggest that the absorption characteristics of cFLG materials are more aligned with the optical properties of graphite pellets rather than those of graphene. It is known that the electronic structure of graphene depends on the number of layers and sheet morphology [61,64]. In particular, graphene surface corrugation was reported to introduce a finite optical band-gap [61] and enhance the

graphene anisotropy, as the charge-carrier transport along and across the folded parts is governed by different effects [65]. However, we must note that TEM, Raman spectroscopy, and Brunauer–Emmett–Teller analyses verified that the sample in this study was indeed crumpled turbostratic few-layer graphene and not graphite [15]. In regards to the particle thickness, using the refractive indices of the plane five-layer graphene sheet [56], though having a similar thickness to the cFLG particles investigated here, did not improve the DDA fit to the experimental data compared to single- and double-layer graphene simulations. Hence, we speculate that the crumpled nature of graphene particles plays a more important role than the thickness in regard to optical properties. It is difficult to quantify the level of particle crumpledness at which optical properties transition from those of graphene to those of graphite. Future experiments aimed at measuring the cFLG active surface area, which correlates with crumpledness, may help to answer this question.

Given the close connection between optical properties and charge transport, this observation also raises the question as to whether the electrical properties of the cFLG are more similar to graphite or defect-free single-layer graphene. We note, however, that the same cFLG sample demonstrated excellent performance when used in Li-ion batteries due to its high electrical conductivity and surface area [16]. Moreover, it has been shown, that the electrical properties of graphene converge to those of graphite only at 11+ layers at room temperature [3,64], while the cFLG particles considered here consist of 5–8 graphene layers.

Further DDA simulations with a smaller wavelength increment (5 nm) were conducted for Particles 1 and 2 to validate the plasmonic response of graphene at UV wavelengths. For these calculations, it was necessary to extrapolate the off-plane refractive index at $\lambda < 300$ nm from the value at $\lambda = 300$ nm, although this is expected to have a negligible effect on the results. Figure 13 shows that both DDA simulations and UV-Vis extinction measurements show a localized surface plasmonic resonance (LSPR) peak, although the latter peak is much broader compared to the one obtained from the DDA results; this can be explained by the wide distribution of cFLG particles size, shape, and random orientation in the suspension. Figure 13 also shows that the DDA predicted extinction peak is blue-shifted compared to the experimental one for all the refractive indices used in this study. Previous extinction measurements on colloidal graphene show this peak to occur between 265–275 nm, which corresponds to π–π^* transitions [40,41]. The blue-shift of the simulated extinction peak could be caused by an inaccurate refractive index of graphene/graphite used in the DDA simulation, or a change in the refractive index in the UV region, which again highlights the necessity for further research on optical properties of cFLG aerosols. Figure 13b shows that the RDG approximation, as expected, cannot reproduce the LSPR peak, highlighting the fact that the electrostatic approximation is not valid for the UV region.

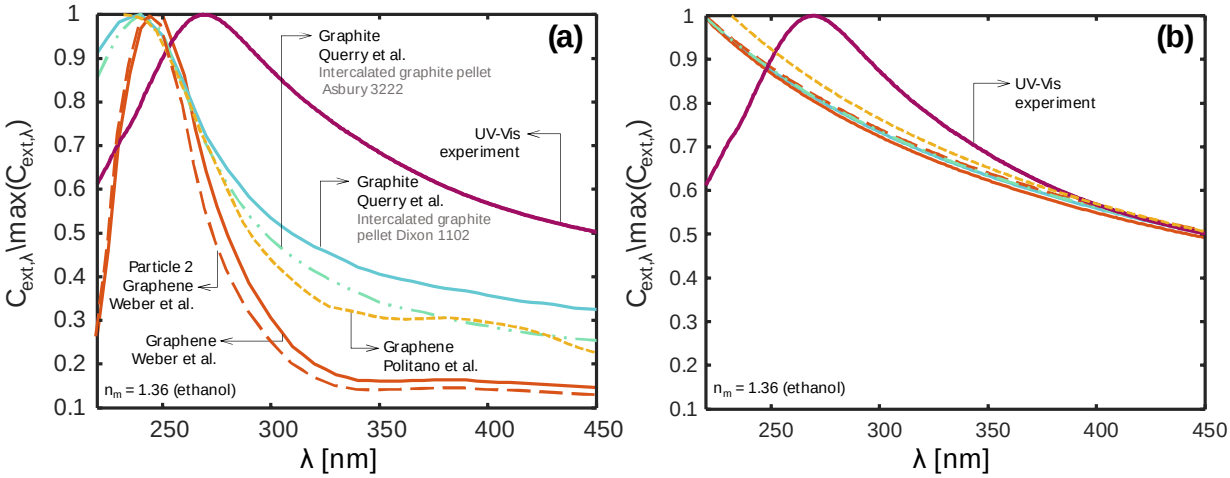

Figure 13. Comparing the experimentally-determined UV-Vis extinction spectrum with spectra found using DDA (a) and RDG (b) simulations and various refractive indices. The DDA predicted extinction peak is narrower and blue-shifted compared to the experimental one. The RDG approximation cannot reproduce the extinction peak.

Conclusions

Crumpled few-layer graphene (cFLG) is one of the most prevalent mass-produced graphene materials, which electronic properties strongly depend on particle morphology. This study correlates the morphology of cFLG particles synthesised in a substrate-free microwave-plasma process from ethanol with their properties measured in cFLG aerosols and colloidal suspensions. A suite of complementary techniques was deployed to analyze particle shape, thickness, lateral size distribution, aspect ratio, mobility, and aerodynamic diameter distributions. The optical properties were assessed in terms of spectrally-resolved extinction coefficients of cFLG suspensions and aerosols, aerosol Ångström exponent, single scattering albedo, and particle mass absorption cross-sections. The results support the evidence of stronger visible light absorption for cFLG aerosols compared to soot aerosols.

DDA simulations were carried out on the tomography-reconstructed cFLG particles to investigate the connection between the optical properties and the morphology and orientation of the particles. Particle orientation has a negligible impact on the normalized absorption efficiency of the particles, and Rayleigh–Debye–Gans (RDG) theory can be used as a reasonable approximation to calculate the cFLG spectral cross-sections. Furthermore, simulated extinction and absorption cross-sections obtained using the refractive indices of graphite more closely resembled those measured with UV-Vis and an aethalometer, rather than single- or few-layer flat graphene. However, additional theoretical and experimental research on the optical properties of crumpled graphene materials is needed.

Further research will follow with the morphology and optical characterization applied on cFLG suspensions and aerosols *in situ* to elucidate the graphene formation and growth kinetics.

Acknowledgments

We gratefully thank S.-A. Lussier, B. Smith, and D. Clavel (all NRC) for technical support, Fadi Araji (Environment and Climate Change Canada) for lending the aethalometer, P. Fortugno (UDE) for providing the cFLG sample and UV-Vis data, M. Heidelmann (CENIDE) for 3D reconstructions, and X. Medvedeva (University of Waterloo) for SEM imaging. This research was enabled in part by support provided by Calcul Québec (www.calculquebec.ca), Shared Hierarchical Academic Research Computing Network (SHARCNET) (www.sharcnet.ca), and Compute Canada (www.computecanada.ca).

Funding

This research was sponsored by the German Research Foundation (Grant 262219004) and the Natural Sciences and Engineering Council (NSERC) Canada Discovery Grant program (RGPIN-2018-03756). S. Musikhin acknowledges funding from the UDE within the International Max Planck Research School RECHARGE.

ORCID

Stanislav Musikhin: 0000-0002-0199-6095

S.T.-Moghaddam: 0000-0003-0892-717X

Joel C. Corbin: 0000-0002-2584-9137

Greg J. Smallwood: 0000-0002-6602-1926

Christof Schulz: 0000-0002-6879-4826

Kyle J. Daun: 0000-0001-9611-7462

References

[1] R. Kumar, S. Sahoo, E. Joanni, R.K. Singh, W.K. Tan, K.K. Kar, A. Matsuda, Recent progress in the synthesis of graphene and derived materials for next generation electrodes of high performance lithium ion batteries, Prog. Energy Combust. Sci. 75 (2019) 100786. 10.1016/j.pecs.2019.100786.

[2] R. Karthick, F. Chen, Free-standing graphene paper for energy application: Progress and future scenarios, Carbon 150 (2019) 292–310. 10.1016/j.carbon.2019.05.017.

[3] A.P. Kauling, A.T. Seefeldt, D.P. Pisoni, R.C. Pradeep, R. Bentini, R.V.B. Oliveira, K.S. Novoselov, A.H. Castro Neto, The Worldwide Graphene Flake Production, Adv. Mater. 30 (44) (2018) 1803784. 10.1002/adma.201803784.
[4] A. Kovtun, E. Treossi, N. Mirotta, A. Scidà, A. Liscio, M. Christian, F. Valorosi, A. Boschi, R.J. Young, C. Galiotis, I.A. Kinloch, V. Morandi, V. Palermo, Benchmarking of graphene-based materials: real commercial products versus ideal graphene, 2D Mater. 6 (2) (2019) 025006. 10.1088/2053-1583/aafc6e.
[5] A. Dato, Graphene synthesized in atmospheric plasmas—A review, J. Mater. Res. 34 (1) (2019) 214–30. 10.1557/jmr.2018.470.
[6] Y. Sun, J. Zhang, Strategies for Scalable Gas-Phase Preparation of Free-Standing Graphene (2020) 20.
[7] S.W. Cranford, M.J. Buehler, Packing efficiency and accessible surface area of crumpled graphene, Phys. Rev. B 84 (20) (2011) 205451. 10.1103/PhysRevB.84.205451.
[8] M. Becton, L. Zhang, X. Wang, On the crumpling of polycrystalline graphene by molecular dynamics simulation, Phys. Chem. Chem. Phys. 17 (9) (2015) 6297–304. 10.1039/C4CP05813E.
[9] Y. Liao, Z. Li, Fatima, W. Xia, Size-dependent structural behaviors of crumpled graphene sheets, Carbon 174 (2021) 148–57. 10.1016/j.carbon.2020.12.006.
[10] A. Ruiz, M.A. Lucherelli, D. Murera, D. Lamon, C. Ménard-Moyon, A. Bianco, Toxicological evaluation of highly water dispersible few-layer graphene in vivo, Carbon (n.d.). 10.1016/j.carbon.2020.08.023.
[11] L. Ou, B. Song, H. Liang, J. Liu, X. Feng, B. Deng, T. Sun, L. Shao, Toxicity of graphene-family nanoparticles: a general review of the origins and mechanisms, Part. Fibre Toxicol. 13 (1) (2016) 57. 10.1186/s12989-016-0168-y.
[12] M. Ema, M. Gamo, K. Honda, A review of toxicity studies on graphene-based nanomaterials in laboratory animals, Regul. Toxicol. Pharmacol. 85 (2017) 7–24. 10.1016/j.yrtph.2017.01.011.
[13] M. Pelin, S. Sosa, M. Prato, A. Tubaro, Occupational exposure to graphene based nanomaterials: risk assessment, Nanoscale 10 (34) (2018) 15894–903. 10.1039/C8NR04950E.
[14] C.D. Zangmeister, R. You, E.M. Lunny, A.E. Jacobson, M. Okumura, M.R. Zachariah, J.G. Radney, Measured in-situ mass absorption spectra for nine forms of highly-absorbing carbonaceous aerosol, Carbon 136 (2018) 85–93. 10.1016/j.carbon.2018.04.057.
[15] S. Musikhin, P. Fortugno, J.C. Corbin, G.J. Smallwood, T. Dreier, K.J. Daun, C. Schulz, Characterization of few-layer graphene aerosols by laser-induced incandescence, Carbon 167 (2020) 870–80. 10.1016/j.carbon.2020.05.052.
[16] A. Münzer, L. Xiao, Y.H. Sehlleier, C. Schulz, H. Wiggers, All gas-phase synthesis of graphene: Characterization and its utilization for silicon-based lithium-ion batteries, Electrochimica Acta 272 (2018) 52–9. 10.1016/j.electacta.2018.03.137.
[17] M. Owen, G. Mulholland, W. Guthrie, Condensation Particle Counter Proportionality Calibration from 1 Particle·cm $^{-3}$ to 10 ^{4} Particles·cm $^{-3}$, Aerosol Sci. Technol. 46 (4) (2012) 444–50. 10.1080/02786826.2011.637998.
[18] A. Wiedensohler, An approximation of the bipolar charge distribution for particles in the submicron size range, J. Aerosol Sci. 19 (3) (1988) 387–9. 10.1016/0021-8502(88)90278-9.
[19] T.J. Johnson, M. Irwin, J.P.R. Symonds, J.S. Olfert, A.M. Boies, Measuring aerosol size distributions with the aerodynamic aerosol classifier, Aerosol Sci. Technol. 52 (6) (2018) 655–65. 10.1080/02786826.2018.1440063.
[20] A. Miller, G. Frey, G. King, C. Sunderman, A Handheld Electrostatic Precipitator for Sampling Airborne Particles and Nanoparticles, Aerosol Sci. Technol. 44 (6) (2010) 417–27. 10.1080/02786821003692063.
[21] B.D.A. Levin, Y. Jiang, E. Padgett, S. Waldon, C. Quammen, C. Harris, U. Ayachit, M. Hanwell, P. Ercius, D.A. Muller, R. Hovden, Tutorial on the Visualization of Volumetric Data Using *tomviz*, Microsc. Today 26 (1) (2018) 12–7. 10.1017/S1551929517001213.

[22] C. Liu, C.E. Chung, Y. Yin, M. Schnaiter, The absorption Ångström exponent of black carbon: from numerical aspects, Atmospheric Chem. Phys. 18 (9) (2018) 6259–73. 10.5194/acp-18-6259-2018.
[23] A. Bescond, J. Yon, F.-X. Ouf, C. Rozé, A. Coppalle, P. Parent, D. Ferry, C. Laffon, Soot optical properties determined by analyzing extinction spectra in the visible near-UV: Toward an optical speciation according to constituents and structure, J. Aerosol Sci. 101 (2016) 118–32. 10.1016/j.jaerosci.2016.08.001.
[24] T.C. Bond, Spectral dependence of visible light absorption by carbonaceous particles emitted from coal combustion, Geophys. Res. Lett. 28 (21) (2001) 4075–8. 10.1029/2001GL013652.
[25] J.C. Corbin, S.M. Pieber, H. Czech, M. Zanatta, G. Jakobi, D. Massabò, J. Orasche, I. El Haddad, A.A. Mensah, B. Stengel, L. Drinovec, G. Mocnik, R. Zimmermann, A.S.H. Prévôt, M. Gysel, Brown and Black Carbon Emitted by a Marine Engine Operated on Heavy Fuel Oil and Distillate Fuels: Optical Properties, Size Distributions, and Emission Factors, J. Geophys. Res. Atmospheres 123 (11) (2018) 6175–95. 10.1029/2017JD027818.
[26] G. Biskos, K. Reavell, N. Collings, Unipolar diffusion charging of aerosol particles in the transition regime, J. Aerosol Sci. 36 (2) (2005) 247–65. 10.1016/j.jaerosci.2004.09.002.
[27] J.C. Corbin, A. Moallemi, F. Liu, S. Gagné, J.S. Olfert, G.J. Smallwood, P. Lobo, Closure between particulate matter concentrations measured ex situ by thermal–optical analysis and in situ by the CPMA–electrometer reference mass system, Aerosol Sci. Technol. (2020) 1–17. 10.1080/02786826.2020.1788710.
[28] J.P.R. Symonds, K.St.J. Reavell, J.S. Olfert, The CPMA-Electrometer System—A Suspended Particle Mass Concentration Standard, Aerosol Sci. Technol. 47 (8) (2013) i–iv. 10.1080/02786826.2013.801547.
[29] T.A. Sipkens, J.S. Olfert, S.N. Rogak, New approaches to calculate the transfer function of particle mass analyzers, Aerosol Sci. Technol. (2019) 1–17. 10.1080/02786826.2019.1680794.
[30] M. Dickau, T. J. Johnson, K. Thomson, G. Smallwood, J. S. Olfert, Demonstration of the CPMA-Electrometer System for Calibrating Black Carbon Particulate Mass Instruments, Aerosol Sci. Technol. 49 (3) (2015) 152–8. 10.1080/02786826.2015.1010033.
[31] T.B. Onasch, P. Massoli, P.L. Kebabian, F.B. Hills, F.W. Bacon, A. Freedman, Single Scattering Albedo Monitor for Airborne Particulates, Aerosol Sci. Technol. 49 (4) (2015) 267–79. 10.1080/02786826.2015.1022248.
[32] International Organization for Standardization (ISO), in Nanotechnologies – Vocabulary – Part 13: Graphene and Related Two-Dimensional (2D) Materials, 2017.
[33] B.K. Ku, P. Kulkarni, Measurement of transport properties of aerosolized nanomaterials, J. Aerosol Sci. 90 (2015) 169–81. 10.1016/j.jaerosci.2015.09.001.
[34] M. Li, R. You, G.W. Mulholland, M.R. Zachariah, Evaluating the Mobility of Nanorods in Electric Fields, Aerosol Sci. Technol. 47 (10) (2013) 1101–7. 10.1080/02786826.2013.819565.
[35] F.J.T. Huber, S. Will, K.J. Daun, Sizing aerosolized fractal nanoparticle aggregates through Bayesian analysis of wide-angle light scattering (WALS) data, J. Quant. Spectrosc. Radiat. Transf. 184 (2016) 27–39. 10.1016/j.jqsrt.2016.06.030.
[36] H. Burtscher, Physical characterization of particulate emissions from diesel engines: a review, J. Aerosol Sci. 36 (7) (2005) 896–932. 10.1016/j.jaerosci.2004.12.001.
[37] S.N. Rogak, R.C. Flagan, H.V. Nguyen, The Mobility and Structure of Aerosol Agglomerates, Aerosol Sci. Technol. 18 (1) (1993) 25–47. 10.1080/02786829308959582.
[38] J.H. Kim, G.W. Mulholland, S.R. Kukuck, D.Y.H. Pui, Slip correction measurements of certified PSL nanoparticles using a nanometer differential mobility analyzer (nano-DMA) for Knudsen number from 0.5 to 83, J. Res. Natl. Inst. Stand. Technol. 110 (1) (2005) 31. 10.6028/jres.110.005.
[39] C.A. Schneider, W.S. Rasband, K.W. Eliceiri, NIH Image to ImageJ: 25 years of image analysis, Nat. Methods 9 (7) (2012) 671–5. 10.1038/nmeth.2089.
[40] S. Uran, A. Alhani, C. Silva, Study of ultraviolet-visible light absorbance of exfoliated graphite forms, AIP Adv. 7 (3) (2017) 035323. 10.1063/1.4979607.

[41] G. Eda, Y.-Y. Lin, C. Mattevi, H. Yamaguchi, H.-A. Chen, I.-S. Chen, C.-W. Chen, M. Chhowalla, Blue Photoluminescence from Chemically Derived Graphene Oxide, Adv. Mater. 22 (4) (2010) 505–9. 10.1002/adma.200901996.
[42] T.C. Bond, R.W. Bergstrom, Light Absorption by Carbonaceous Particles: An Investigative Review, Aerosol Sci. Technol. 40 (1) (2006) 27–67. 10.1080/02786820500421521.
[43] C. Backes, K.R. Paton, D. Hanlon, S. Yuan, M.I. Katsnelson, J. Houston, R.J. Smith, D. McCloskey, J.F. Donegan, J.N. Coleman, Spectroscopic metrics allow in situ measurement of mean size and thickness of liquid-exfoliated few-layer graphene nanosheets, Nanoscale 8 (7) (2016) 4311–23. 10.1039/C5NR08047A.
[44] R. Dastanpour, A. Momenimovahed, K. Thomson, J. Olfert, S. Rogak, Variation of the optical properties of soot as a function of particle mass, Carbon 124 (2017) 201–11. 10.1016/j.carbon.2017.07.005.
[45] F. Liu, J. Yon, A. Fuentes, P. Lobo, G.J. Smallwood, J.C. Corbin, Review of recent literature on the light absorption properties of black carbon: Refractive index, mass absorption cross section, and absorption function, Aerosol Sci. Technol. 54 (1) (2020) 33–51. 10.1080/02786826.2019.1676878.
[46] L. Fierce, T.B. Onasch, C.D. Cappa, C. Mazzoleni, S. China, J. Bhandari, P. Davidovits, D.A. Fischer, T. Helgestad, A.T. Lambe, A.J. Sedlacek, G.D. Smith, L. Wolff, Radiative absorption enhancements by black carbon controlled by particle-to-particle heterogeneity in composition, Proc. Natl. Acad. Sci. 117 (10) (2020) 5196–203. 10.1073/pnas.1919723117.
[47] G.A. Kelesidis, C.A. Bruun, S.E. Pratsinis, The impact of organic carbon on soot light absorption, Carbon 172 (2021) 742–9. 10.1016/j.carbon.2020.10.032.
[48] H. DeVoe, Optical Properties of Molecular Aggregates. I. Classical Model of Electronic Absorption and Refraction, J. Chem. Phys. 41 (2) (1964) 393–400. 10.1063/1.1725879.
[49] Purcell, Pennypacker, Scattering and absorption of light by nonspherical dielectric grains, Astrophys. J. 186 (2) (1973) 705–14.
[50] C.M. Sorensen, Light Scattering by Fractal Aggregates: A Review, Aerosol Sci. Technol. 35 (2) (2001) 648–87. 10.1080/02786820117868.
[51] L.A. Falkovsky, Optical properties of graphene and IV–VI semiconductors, Phys.-Uspekhi 51 (9) (2008) 887–97. 10.1070/PU2008v051n09ABEH006625.
[52] V.G. Kravets, A.N. Grigorenko, R.R. Nair, P. Blake, S. Anissimova, K.S. Novoselov, A.K. Geim, Spectroscopic ellipsometry of graphene and an exciton-shifted van Hove peak in absorption, Phys. Rev. B - Condens. Matter Mater. Phys. 81 (15) (2010) 1–6. 10.1103/PhysRevB.81.155413.
[53] J.W. Weber, V.E. Calado, M.C.M. Van De Sanden, J.W. Weber, V.E. Calado, M.C.M. Van De Sanden, Optical constants of graphene measured by spectroscopic ellipsometry Optical constants of graphene measured by spectroscopic ellipsometry 091904 (2010) (2015) 1–4. 10.1063/1.3475393.
[54] G.G. Politano, C. Vena, G. Desiderio, C. Versace, Variable angle spectroscopic ellipsometry characterization of turbostratic CVD-grown bilayer and trilayer graphene, Opt. Mater. 107 (March) (2020) 110165. 10.1016/j.optmat.2020.110165.
[55] E. Ochoa-Martínez, M. Gabás, L. Barrutia, A. Pesquera, A. Centeno, S. Palanco, A. Zurutuza, C. Algora, Determination of a refractive index and an extinction coefficient of standard production of CVD-graphene, Nanoscale 7 (4) (2015) 1491–500. 10.1039/c4nr06119e.
[56] Z. Pápa, J. Csontos, T. Smausz, Z. Toth, J. Budai, Spectroscopic ellipsometric investigation of graphene and thin carbon films from the point of view of depolarization effects, Appl. Surf. Sci. 421 (2017) 714–21. 10.1016/j.apsusc.2016.11.231.
[57] E.H.L. Djurišić, Aleksandra B., Optical properties of graphite, J. Microsc. 85 (10) (1999) 7404–10. 10.1111/j.1365-2818.1977.tb01142.x.
[58] M.R. Querry, Optical Constants, 1985.
[59] F. Wooten, Optical Properties of Solids, ACADEMIC PRESS, INC., New York, 1972.

[60] C. Pecharromán, G. Mata-Osoro, L.A. Díaz, R. Torrecillas, J.S. Moya, On the transparency of nanostructured alumina: Rayleigh-Gans model for anisotropic spheres, Opt. Express 17 (8) (2009) 6899. 10.1364/oe.17.006899.
[61] S. Deng, V. Berry, Wrinkled, rippled and crumpled graphene: an overview of formation mechanism, electronic properties, and applications, Mater. Today 19 (4) (2016) 197–212. 10.1016/j.mattod.2015.10.002.
[62] K.-K. Bai, Y. Zhou, H. Zheng, L. Meng, H. Peng, Z. Liu, J.-C. Nie, L. He, Creating One-Dimensional Nanoscale Periodic Ripples in a Continuous Mosaic Graphene Monolayer, Phys. Rev. Lett. 113 (8) (2014) 086102. 10.1103/PhysRevLett.113.086102.
[63] S. Talebi-Moghaddam, F.J. Bauer, F.J.T. Huber, S. Will, K.J. Daun, Inferring soot morphology through multi-angle light scattering using an artificial neural network, J. Quant. Spectrosc. Radiat. Transf. 251 (2020) 106957. 10.1016/j.jqsrt.2020.106957.
[64] B. Partoens, F.M. Peeters, From graphene to graphite: Electronic structure around the K point, Phys. Rev. B 74 (7) (2006) 075404. 10.1103/PhysRevB.74.075404.
[65] W. Zhu, T. Low, V. Perebeinos, A.A. Bol, Y. Zhu, H. Yan, J. Tersoff, P. Avouris, Structure and Electronic Transport in Graphene Wrinkles, Nano Lett. 12 (7) (2012) 3431–6. 10.1021/nl300563h.